

Birefringence in a Silicon Beamsplitter at 2 μ m for Future Gravitational Wave Detectors

Alex Adam, Carl Blair, Chunrong Zhao
OzGrav, University of Western Australia.
 (Dated: November 1, 2024)

The next generation of gravitational wave detectors will move to cryogenic operation in order to reduce thermal noise and thermal distortion. This necessitates a change in mirror substrate with silicon being a good candidate. Birefringence is an effect that will degrade the sensitivity of a detector and is of greater concern in silicon due to its crystalline nature. We measure the birefringence in a $\langle 100 \rangle$ float zone silicon beamsplitter since we expect there to be a large inherent birefringence due to the spatial dispersion effect. We observe that the birefringence varied between $3.44 \pm 0.12 \times 10^{-7}$ and $1.63 \pm 0.05 \times 10^{-7}$ and estimate the birefringence along the $\langle 110 \rangle$ axis to be $1.64 \pm 0.5 \times 10^{-6}$ at $2\mu\text{m}$. We demonstrate this effect and argue that it strengthens the case for $2\mu\text{m}$ and $\langle 100 \rangle$ silicon.

I. INTRODUCTION

Gravitational waves detectors have proved capable of performing measures of the gravitational waves emitted from the mergers of compact binaries[1]. The current second-generation gravitational wave detectors will be replaced in the upcoming decade by a new generation that takes advantage of a wide array of new technologies. The current limiting noise sources of gravitational wave detectors are quantum shot-noise at high frequencies, thermal noise in the centre of the detection band and a combination of quantum radiation pressure noise and seismic noise and related phenomena at low frequencies[2]. It is clear then that a reduction in quantum noise and thermal noise will prove advantageous in lowering the noise across much of the detection band. Future detectors will aim to combat quantum shot noise by increasing the arm power of the detectors, and increasing the level of squeezed vacuum injection[3, 4]. This will increase the thermal energy absorbed by the test mass which creates thermal distortion caused by the thermo-elastic and thermo-optic effects. To reduce thermal noise new mirror substrate materials must be used and cryogenic temperatures are being explored. The optics in the aLIGO and aVIRGO detectors use a fused silica substrate[2, 5]. This is chosen for its low absorption at 1064nm and its high mechanical quality factor. The requirement for the high mechanical quality factor originates with the fluctuation-dissipation theorem which links the mechanical loss of a system to its thermal noise spectrum[6]. Fused silica however, loses its high Q factor as it is cooled to cryogenic temperature which means that simply reducing that temperature without a change in substrate material will lead to a net increase in thermal noise. We therefore require that future cryogenic detectors will require optic substrates that have a high Q at cryogenic temperatures and well as good thermal conductivity, low thermal expansion and low thermo-optic effect to reduce thermal effects. One such material is silicon, with a Q of 10^8 at cryogenic temperatures, a high thermal conductivity of 137W/mK , and two temperatures where the coefficient of thermal ex-

pansion is 0 at 18K and 123K [7, 8]. However, silicon has a high absorption at 1064nm and so a change in wavelengths is required, with there being two candidates of 1550nm and 2000nm.

There are numerous factors that affect the decision between laser wavelengths. 1550nm has a lower absorption in the silicon test mass as well as more mature technology that can aid in quantum noise suppression. 2000nm has lower absorption in the proposed high reflective coatings as well as reduced scattering loss and as demonstrated in this paper, birefringence. The LIGO Voyager white paper has concluded that this coating absorption is the most important factor and has led to then selecting a wavelength of around 2000 nm[3]. One currently unresolved design choice in 2 μm detectors is the choice of beam splitter material. In this paper we investigate birefringence in silicon beam splitters. We use a $2\mu\text{m}$ apparatus with photoelastic modulation to measure the birefringence as a function of crystal axis to show that as a beam splitter, float zone silicon will be spatial dispersion limited.

A. Birefringence

The origin of the favourable thermal properties of silicon rests in its crystal structure, however this is also a key area of concern. As a crystalline material silicon introduces an abundance of properties that are concerned with the symmetries of the crystal structure. One of these is birefringence, which in a detector will introduce losses which can reduce the efficacy of power recycling and degrade the squeezing of quantum noise. It is estimated that the level of acceptable birefringence for Einstein telescope is 10×10^{-8} in the case of a optic that cannot have its optic axes aligned to the input polarisation or 10×10^{-7} in the case of a well aligned optic which corresponds to a 1% optical loss limit.[9] If we assume a 0.1% optical loss allowance due to beamsplitter birefringence using the same approach, and allow for a stress birefringence level of 4×10^{-8} (justified below) then

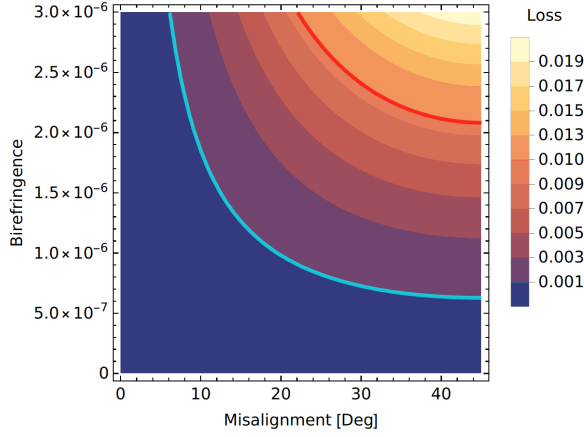


Figure 1: Loss from depolarisation in a silicon beamsplitter 6cm in length at $2\mu m$. The cyan contour shows 0.1% loss and the red shows 1% loss. This does not take account of other birefringence related effects and therefore should be viewed as an indicative upper limit. The thickness of the beamsplitter is based on the parameters for the aLIGO beamsplitter [2].

this produces the limit shown in cyan in figure 1.

Birefringence refers to an optical anisotropy in which a material comes to possess optical axes. Depending on the alignment of the input polarisation to these optical axes, the output light will be elliptically polarised to some extent. The most commonly observed form of birefringence, sometimes referred to as gyrotropy, is due to asymmetry in the crystal structure. This is the origin of birefringence in sapphire and calcite. Silicon is a cubic crystal and therefore non-gyrotropic but some birefringence can be induced if the crystal symmetry is distorted by the application of stress. We have previously measured the stress induced birefringence in the same sample. However when we consider higher order effects cubic crystals will display a birefringence. Specifically the cubic becomes optically heptaxial with optical axes aligned with the face normals and corner diagonals. We refer to this effect as “spatial dispersion” since it is using the assumptions of spatial dispersion that allows us to derive the effect.

Spatial dispersion can be understood when we compare it to frequency dispersion. We use two quantities to describe a plane wave, the frequency and the wavenumber (and associated wave vector). In order to describe the phase shift imparted to a time varying magnetic field when it passes through a material we can not only look at amplitude at a single moment in time. We must look at the field over all times, or in another way of thinking about the problem we look at the signal in the frequency domain and so take the fourier transform[10].

$$E(\mathbf{r}, \omega) = \frac{1}{2\pi} \int_{-\infty}^{\infty} E(\mathbf{r}, t) e^{i\omega t} dt \quad (1)$$

Likewise, we cannot simply look at the electric field at one single location, but instead we must take the effect

of the electric field at all locations into account. This is the same as taking the spatial fourier transform and means that the dielectric tensor now has a wave vector dependence[10].

$$E(\mathbf{k}, \omega) = \frac{1}{(2\pi)^4} \int_{-\infty}^{\infty} \int_{-\infty}^{\infty} E(\mathbf{r}, t) e^{-i(\mathbf{k} \cdot \mathbf{r} - \omega t)} d\mathbf{r} dt \quad (2)$$

The effect of this is that cubic crystals are no longer ideally isotropic and will exhibit a weak anisotropy. If we are far away from quadrupole transitions then we can say that this anisotropy has a wavelength dependence of the inverse square of the wavelength. Therefore a longer wavelength will reduce the effect, this provides additional support for the use of a wavelength in the 2um range.

Traditionally we make the assumption that materials are isotropic, this approximation works well for some of the most commonly used optical substrates such as fused silica. These materials, when there are no external forces, show no dependence on the direction of light propagation. However, in the case of crystal optics we cannot use this approximation. Crystals have a regularly structured lattice that must be taken into account. The effect of the lattice structure is that the polarisability of the crystal is modulated at certain spatial frequencies. We can account for this by using an expansion of the dielectric tensor in terms of powers of the wave vector, with each power being multiplied by a tensor to account for the symmetries present at each length scale[10]:

$$\epsilon(\omega, \mathbf{k})_{ij} = \epsilon(\omega)_{ij} + i\gamma(\omega)_{ijl}k_l + \alpha(\omega)_{ijlm}k_lk_m + \dots \quad (3)$$

or using the reciprocal of the tensor:

$$\epsilon^{-1}(\omega, \mathbf{k})_{ij} = \epsilon^{-1}(\omega)_{ij} + i\delta(\omega)_{ijl}k_l + \beta(\omega)_{ijlm}k_lk_m + \dots \quad (4)$$

The zeroth-power of the wave vector is the isotropic term, $\epsilon(\omega)_{ij}$, which accounts for the averaged effect in all directions. This is the dominant term of order unity in many materials. The first power, γ_{ij} and δ_{ij} , accounts for “gyrotropy” which is the birefringence effect that occurs in crystals without a centre of symmetry. This effect is responsible for the double refraction of materials such as calcite. In crystals that possess a centre of symmetry, ie. cubic crystals, this tensor has all elements equal to zero. An important result occurs when we consider the quadratic term which has a tensor, α_{ij} and β_{ij} , that in cubic crystals takes the same form as the photoelastic tensor[10].

$$\beta = \begin{pmatrix} \beta_{11} & \beta_{12} & \beta_{12} & 0 & 0 & 0 \\ \beta_{12} & \beta_{11} & \beta_{12} & 0 & 0 & 0 \\ \beta_{12} & \beta_{12} & \beta_{11} & 0 & 0 & 0 \\ 0 & 0 & 0 & \beta_{44} & 0 & 0 \\ 0 & 0 & 0 & 0 & \beta_{44} & 0 \\ 0 & 0 & 0 & 0 & 0 & \beta_{44} \end{pmatrix} \quad (5)$$

In practical terms this means that cubic crystals are not optically isotropic but in fact display a weak anisotropy. Since this effect occurs with the quadratic wave vector

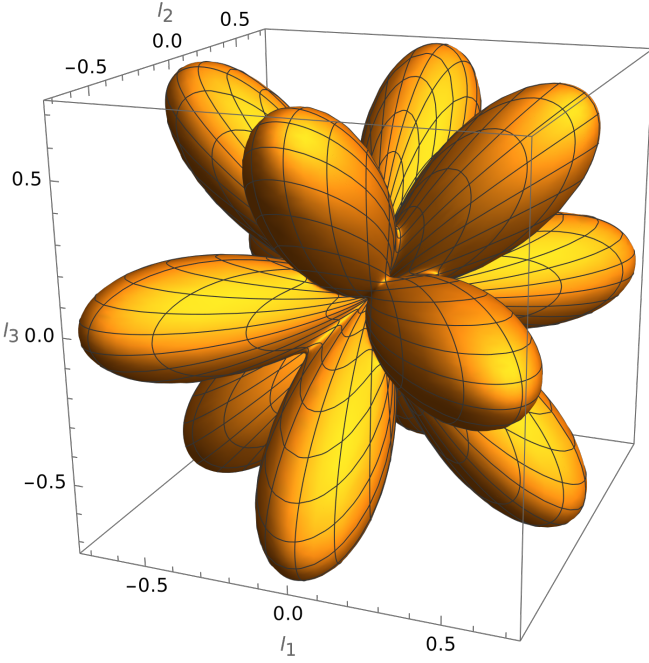


Figure 2: 3D plot of the direction dependence of the birefringence introduced by considering spatial dispersion. Note the maxima at the $\langle 110 \rangle$ axes and the minima at the $\langle 100 \rangle$ and $\langle 111 \rangle$ axes. There are also saddle points present at the $\langle 211 \rangle$ axes. The birefringence has been normalised to a maximum of 1.

term it means that the magnitude of the contribution will be proportional to the inverse square of the wavelength. The direction dependence of the magnitude of the spatial dispersion normalised to 1 is given by[11]:

$$\Delta n_{SD} = 4\sqrt{(l_1^2 l_2^2 + l_1^2 l_3^2 + l_2^2 l_3^2)^2 - 3l_1^2 l_2^2 l_3^2} \quad (6)$$

Where l_1, l_2 , and l_3 are the direction cosines given by $l_1 = \sin \theta \cos \phi$, $l_2 = \sin \theta \sin \phi$ and $l_3 = \cos \theta$. This is plotted in figure 2 where it can be seen that there are maxima at the face diagonals and minima at the face normals and corner diagonals. In the case of an input test mass there beam travels only along a single direction and so the test mass can be manufactured so that the optical path aligns with the $\langle 100 \rangle$ or $\langle 111 \rangle$ axis. In the case of a beam splitter it is not so simple.

The transmitted beam through the beamsplitter will be refracted to 0.2 rad (12°) from normal. Recombined beam will be transmitted through the substrate at 0.2 rad to the other side of normal, making a 0.4 rad (24°) difference between incoming and outgoing beams. This means that the silicon optic will show a spatial dispersion effect of around between 7 – 15% of the maximum spatial dispersion effect for a $\langle 100 \rangle$ oriented optic, see figure 3. The case of the $\langle 111 \rangle$ optic is much more severe since the spatial dispersion will be between 28 – 43% of the maximum level. This is further complicated by the

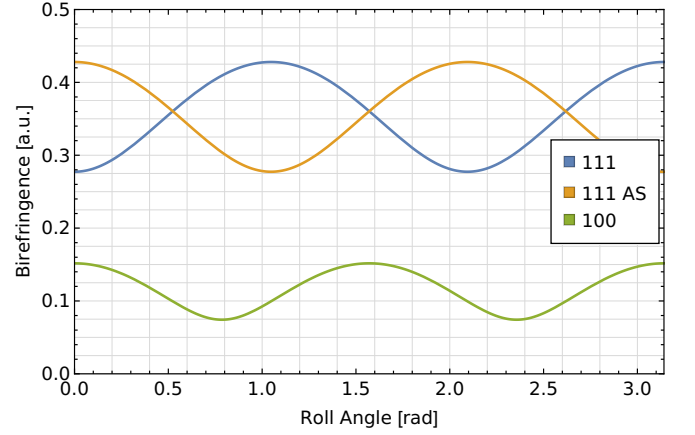


Figure 3: Change in Birefringence as a $\langle 100 \rangle$ and $\langle 111 \rangle$ silicon beamsplitter is rolled around its central axis. Note that the birefringence is lowest at roll angle of 45° . The birefringence has been normalised so that birefringence along the $\langle 110 \rangle$ axis is 1. The arm-transmitted beam and the AS transmitted beam in the case of $\langle 100 \rangle$ experience the same birefringence due to the 4-fold symmetry. The two beams in a $\langle 111 \rangle$ beamsplitter experience different birefringence levels due to the 3-fold symmetry.

threefold symmetry of the $\langle 111 \rangle$ axis which means that that when the beam transmitted to the arm experiences a birefringence of 28% the beam transmitted towards the antisymmetric port will experience a birefringence of 43% of the maximum. It is also possible to produce an optic that has been cut so that one of the transmitted beams will be along one of the zero birefringence axes. However, this comes at a trade-off since of the other transmitted beam with experience much high birefringence. It will be necessary to consider if a large birefringence in the anti-symmetric port is acceptable for no spatial dispersion induced birefringence in the arms. An exploration of some possible cuts is presented in figure 4, the two beams are separated by a roll angle of π . The saving grace here is that because the spatial dispersion effect is intrinsically linked to the crystal axes it will be possible to align the optic axes so that the effect is almost entirely removed. This however means that alignment for the reduction of stress birefringence will, in general, be impossible. This also introduces a much higher dependency on the quality of the crystal and the homogeneity of the crystal axes. Therefore it is necessary to conduct measurements on silicon to measure the spatial dispersion birefringence in the case of a beamsplitter. By observing the changing birefringence pattern as we rotate the test mass around its central axis we can estimate spatial dispersion effect at $2\mu\text{m}$ and draw conclusions about the best orientation for a test mass to minimise the spatial dispersion birefringence.

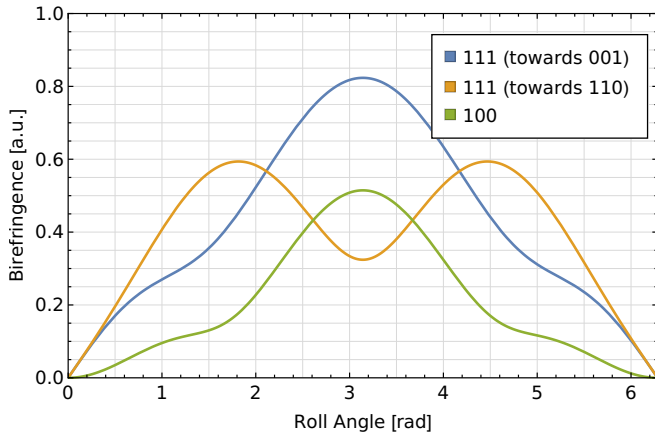


Figure 4: Birefringence with roll angle in a beamsplitter that has been cut so that the one of the transmitted beams will experience no spatial dispersion contribution to the birefringence. The cuts have been made at 0.2 rad from the specified crystal axis. There are two separate cases for the a $\langle 111 \rangle$ beamsplitter since the cut can be made towards the $\langle 001 \rangle$ axis or towards the $\langle 110 \rangle$ axis. The two beams will be separated by a roll angle of π .

II. PREVIOUS MEASUREMENTS

Pastrnak and Vedam made measurements of spatial dispersion in silicon in 1970 using two rectangular samples of silicon that had all faces polished[12]. They used a polariser-analyser set up with a chopped beam. They carried out there experiments at $1.15\mu\text{m}$ and found values for the difference between the birefringence on the non-birefringent axes. They measured the birefringence at the $\langle 110 \rangle$ axis to be 5×10^{-6} . This was the only measurement in birefringence until after the year 2000 since it was not an effect that was observable in most situations. The resurgence in spatial dispersion came when those working with UV optics noticed that their supposedly non-birefringent cubic crystals had very large birefringences. This is because the spatial dispersion effect is much larger at lower wavelengths.

In 2001, Burnett, Levine and Shirley carried out a series of *ab initio* calculations of the spatial dispersion effect for several cubic crystals including silicon and compared these to the existing measurements[13]. From both the work of Burnett *et al* and from Pastrnak and Vedam it is very clear that the wavelength dependence of the spatial dispersion effect is very high. This is not surprising when we remember that it is proportional to $(a/\lambda)^2$ where a is the characteristic length of the crystal.

In 2002, Chu *et al* measured that spatial dispersion in silicon at $1.52\mu\text{m}$ with dislocation free silicon ingots[14]. They found that the spatial birefringence was at a level of 3.2×10^{-6} . This is close to the measurements of Pastrnak and Vedam using a $1/\lambda^2$ relationship. From these measurements we can extrapolate the expected value of spa-

tial dispersion at $2\mu\text{m}$ which is between $1.65 - 1.85 \times 10^{-6}$ in the case of the $\langle 110 \rangle$ axis.

III. METHODOLOGY

A. Sample Set-up and Control

The sample of silicon used for these measurements was a cylindrical piece of float-zone silicon 10 cm in diameter and 3 cm in length (see figure 5). The central axis was collinear with the $\langle 100 \rangle$ crystallographic axis. The front and back surfaces had been polished with the front surface having a radius of curvature of 44m and the back surface being planar with a wedge. The sample is one of a set of three created in order to be used as test masses in a suspended optical cavity experiment. For this reason the sample has flat sides with a pair of holes in each side which will be used to anchor the suspension points. The sample was previously used in measurements of stress induced birefringence to evaluate the suitability of silicon as an input test mass substrate[15]. In these measurements the test mass central axis was aligned with the beam axis. In order to investigate the birefringence in the beamsplitter case the translation stage that the test mass sat on was rotated so that the central axis of the sample was at a 45 degree angle to the propagating beam. In order to reduce the effect of stress the sample was placed in a mount that was designed to produce an even stress distribution and to ensure that the stress distribution would not change between repeat measurements. The mount, shown in figure 6, was designed to rotate the test mass around the central axis, this was necessary so as to fully characterise the spatial dispersion birefringence. This mount consists of an inner and outer ring made of aluminium which can rotate with respect to one another. The mount contains a layer of foam wrapped in plastic to hold the sample. The rotation of the mount was adjusted by hand between measurements. The mount was then mounted on a translation stage built from a modified 3D printer. The translation stage was oriented such that the plane of motion intersected the beam at a 45 degree angle. Control of the translation stage was via a python script using the REQUESTS library to send commands to a RaspberryPi running an OctoPi server which was connected to the translation stage.

B. Optical Set-up

The optical set-up for measuring birefringence is based on that described by Wang and Oakberg which uses two polarisers and a photoelastic modulator (PEM) (see figure 7). The beam passes through the first polariser which is set to 45 degrees to the slow axis of the PEM. It then travels through the PEM which modulates the ellipticity of the light at 50kHz. The light then travels through the sample and the birefringence inherent in the sample

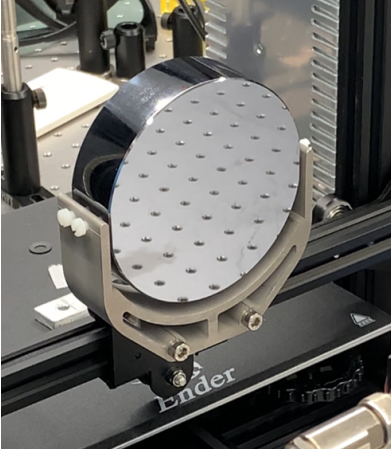


Figure 5: $< 100 >$ float zone silicon sample used in these measurements.

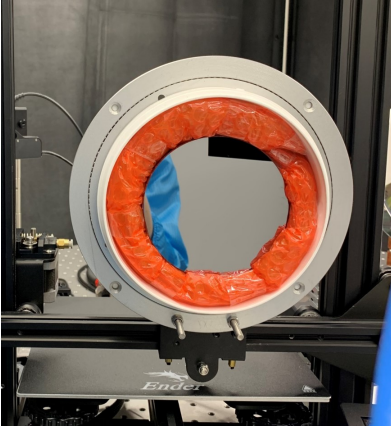


Figure 6: Silicon sample placed in rotation mount and mounted onto the translation stage.

modifies the 50 kHz signal. The second polariser is then set to 0 degrees or 45 degrees and then the beam is measured using a photodetector. The strength of the 50kHz signal is extracted using a fast fourier transform which is then normalised by the DC signal which gives:

$$\frac{V_{ch1}(1f)}{DC_{ch1}} = \delta \cos(2\rho) \frac{\sqrt{2}J_1(\Delta_0)}{1 - J_0(\Delta_0)} \quad (7)$$

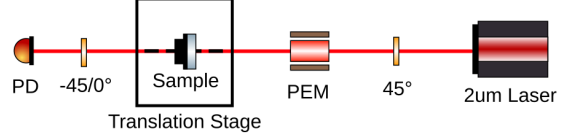
$$\frac{V_{ch2}(1f)}{DC_{ch2}} = \delta \sin(2\rho) \sqrt{2}J_1(\Delta_0) \quad (8)$$

where $V_{chx}(1f)$ is the 50 kHz signal, DC_{chx} is the DC signal, δ is the phase shift, ρ is the slow axis angle and Δ_0 is the retardation of the PEM. We can then define R_{ch1} and R_{ch2} as:

$$R_{ch1} = \frac{V_{ch1}(1f)}{DC_{ch1}} \frac{1 - J_0(\Delta_0)}{2J_1(\Delta_0)} \sqrt{2} = \delta \cos(2\rho) \quad (9)$$

$$R_{ch2} = \frac{V_{ch2}(1f)}{DC_{ch2}} \frac{1}{2J_1(\Delta_0)} \sqrt{2} = \delta \sin(2\rho) \quad (10)$$

ITM Configuration



Beamsplitter Configuration

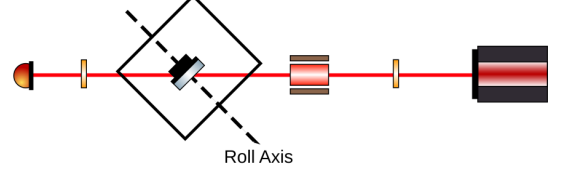


Figure 7: Experimental set up showing the difference between the measuring the birefringence in a beamsplitter and the background birefringence caused by internal and external stresses.

Which we can use to is possible to find the phase shift and angle:

$$\delta = \sqrt{(R_{ch1})^2 + (R_{ch2})^2} \quad (11)$$

$$\rho = \frac{1}{2} \arctan\left(\frac{R_{ch2}}{R_{ch1}}\right) \quad (12)$$

Which gives the birefringence as:

$$\Delta n = \frac{\lambda}{2\pi d} \delta \quad (13)$$

where λ is the laser wavelength and d is the optic thickness.

C. Data Processing

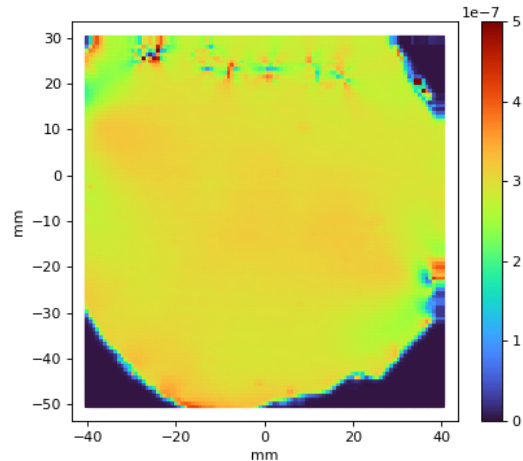
The measurements are taken using a National Instruments data acquisition box using the National Instruments Python API. The analyser is placed in a Thorlabs motorised mount and connected to a Thorlabs Motor Controller. The Motor Controller can be controlled via the Thorlabs Kinesis dotNET API from a Python script using the python.NET library. The 50kHz signal is extracted using the SciPy Welch spectral density estimate and the results are plotted using Matplotlib. These functions are all controlled from a single python script running on the Lab PC which means that the process is almost entirely automated. For the 10000 point scans included in this paper the runtime was around 24 hrs. Each point measurement consisted of a three second measurement at 1.4 Msamples/s. This was experimentally found to be a good sample rate and time for recovering known signals.

IV. RESULTS

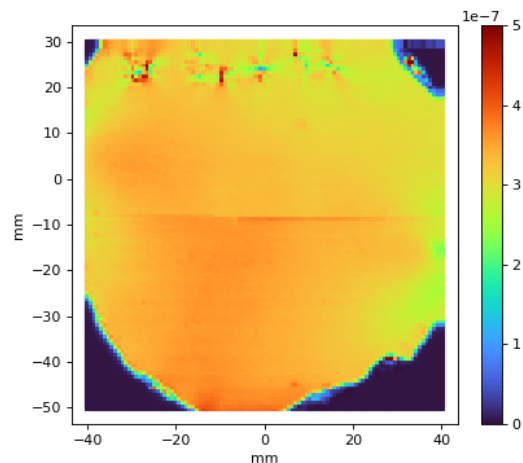
We conducted nine measures at different roll angles from -20° to 90° (figure 8). Angles are referenced from the mounting orientation based on the suspension points. These scans were completed over a 100×100 point grid which allowed for very high spatial resolution. We also conducted 9 measurements of the background birefringence from -20° to 90° with the sample surface normal to the incident light which allowed us to characterise the stress introduced by the new mount. We did not observe a strong roll dependence on the background stress with variation being within 1 standard deviation. In order to compare measurements an average was taken as a box of 40×40 points in the centre of the test mass (figure 9). The change in birefringence with the roll angle shows a clear sinusoidal pattern which matches what we would expect from theory. The minimum occurs at 35° at a value of $1.63 \pm 0.05 \times 10^{-7}$ and at a maximum of $3.44 \pm 0.12 \times 10^{-7}$ at -10° . This produces an angular separation of minimum and maximum of 45° as expected. The background birefringence level was measured to be between $1.6 - 4.7 \times 10^{-8}$ and was subtracted from the measurements and fitted to equation 6 which gives us a value for the maximum spatial dispersion induced birefringence (birefringence in $< 110 >$ direction) of $1.64 \pm 0.05 \times 10^{-6}$ (see figure 10). This is consistent with the measurements made by Pastrnak and Vedom using the $\frac{1}{\lambda^2}$ relation[12]. The measurements made by Chu *et al* are not difficult to compare as no experimental error is given. The fitting also suggests that the crystal axes are rolled $13^\circ \pm 2^\circ$ degrees clockwise as viewed looking at the front surface. This is likely due to imprecision in the machining process and is of no great concern, however, if this were intended as a silicon beam splitter this may prove a severe error. These measurements demonstrate that silicon could be used as a beam splitter if the input polarisation is within 4 degrees of the optic axes. This demonstrates the importance of the well defined and consistent crystal axes throughout the optic. Visible in all of the measurements are the high birefringence artefacts that occur in the upper left quadrant of the test mass. The points were first noted when Jaberian Hamedan *et al* conducted stress induced birefringence scans of the sample[15]. These can be seen to rotate in concert with the test mass which demonstrates that they are of physical significance. The horizontal features present on the scans are measurement artefacts.

V. CONCLUSION

If silicon is going to be used as a beamsplitter substrate in future gravitational wave detectors then great care will need to be taken with alignment of the optic and the polarisation. We demonstrated that the test mass crystal axis were not aligned to the test mass geometric axes which if not controlled for would cause significant diffi-

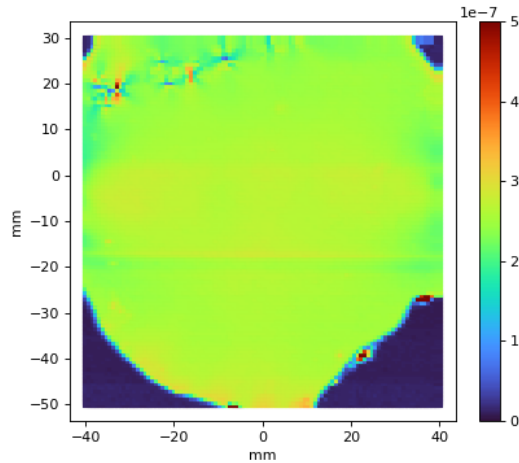


(a) -20° Roll

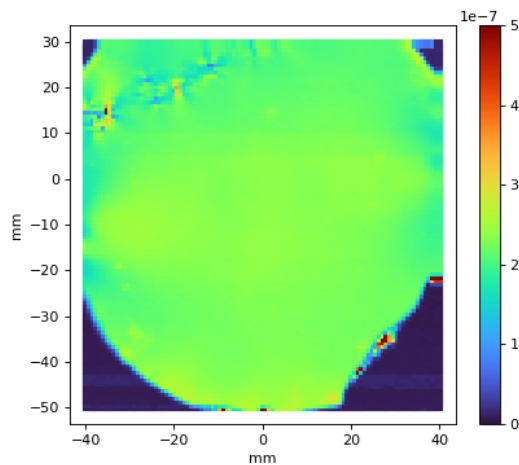


(b) -10° Roll

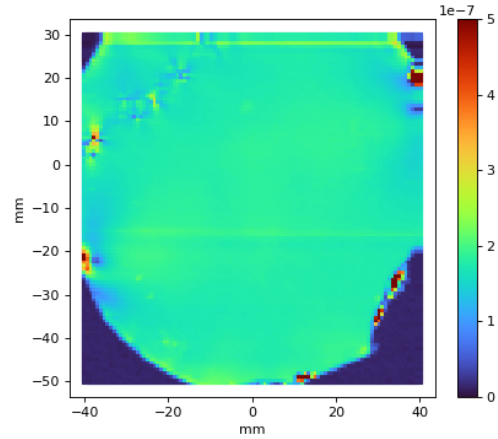
culties in a beamsplitter. The spatial dispersion effect raises that birefringence level of a $< 100 >$ beamsplitter by $\approx 1 - 3 \times 10^{-7}$ compared to the same optic being used as an input test mass. This is still at an acceptable level especially if alignment can be carefully controlled and if the optic is oriented to the minimum birefringence direction. We may also consider the option of cutting the optic so that the light can be transmitted along the non-birefringent axes. For a 45° optic the beam will propagate at 11.5° away from the normal, this means that the light transmitted towards the x-arm and the light transmitted towards the antisymmetric port will be separated by 23° and so simply changing the cut direction will not remove the effect of the birefringence. It may be possible to introduce compensation optics into the power recycling cavity. The spatial dispersion effect is a homogeneous effect so it would be simpler to compensate for the effect than for a complex birefringence pattern. This would possibly not be desirable due to the increase in thermal



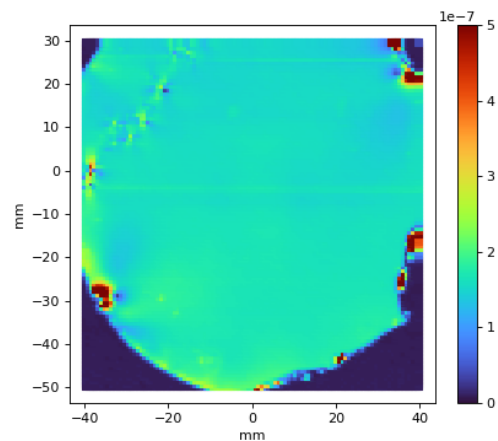
(c) 0° Roll



(d) 10° Roll



(e) 22° Roll



(f) 35° Roll

noise as well any extra birefringence contributed by imperfections in the compensation scheme. Any scheme of this sort would require experimental testing to evaluate its efficacy. This study also reinforces the importance of high resolution scans of any optics, a scan of low resolution or only a single point would not have measured the high-birefringence points that can be seen close to the edge of the test mass. These were likely introduced during the manufacturing of the crystal. Our measurements also offer support for using $\langle 100 \rangle$ silicon and $2\mu\text{m}$ light in the detector. This is because a $\langle 111 \rangle$ beamsplitter will produce a larger birefringence due to the fact that the $\langle 111 \rangle$ zero birefringence point is a zero crossing whereas the $\langle 100 \rangle$ is a local minimum. The inverse square dependence on wavelength supports

$2\mu\text{m}$ over 155nm which will experience a 60% increase in birefringence. Ultimately we have demonstrated that silicon is a plausible beamsplitter substrate materials, however the requirements for its use are significantly stricter

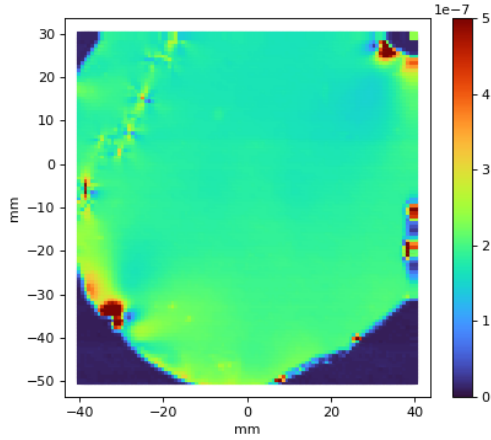
than for an test mass.

VI. ACKNOWLEDGMENTS

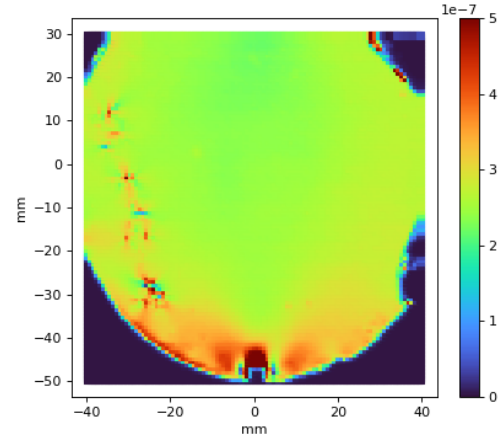
The authors would like to thank the members of the UWA gravitational wave instrumentation group for their useful and insightful feedback over the course of this project. The authors would also like to thank Professor Li Ju and Felix Wojcik for their help in constructing the rotation mount. This work was supported by the Australian Research Council Centre of Excellence for Gravitational Wave Discovery (CE230100016).

[1] B. P. Abbott, R. Abbott, T. D. Abbott, M. R. Abernathy, F. Acernese, K. Ackley, C. Adams, T. Adams,

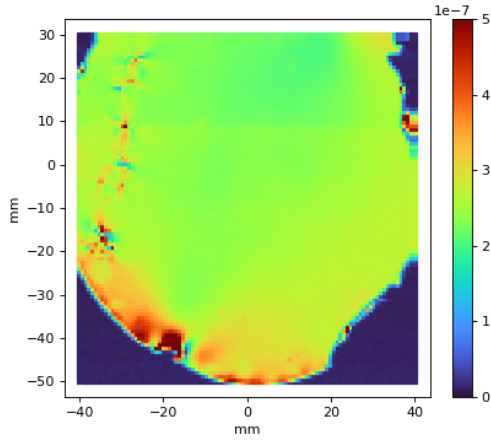
P. Addesso, J. B. Camp, and L. P. Singer, Observation



(g) 45° Roll



(i) 90° Roll



(h) 67° Roll

Figure 8: Ten thousand point scans of the birefringence in the silicon test mass in a beamsplitter orientation as it is rolled around its central axis from -20° to 90° with respect to its mounting orientation. The horizontal artefacts present are not real an only an effect of the measurment apparatus. The irregular shape around the sides of the test mass is due to the beam being blocked by the foam that surrounds it. The high birefringence that occurs directly over the machined holes should not be taken as real.

of gravitational waves from a binary black hole merger, *Physical review letters* **116**, 061102 (2016).

- [2] R. Abbott, P. Addesso, N. Aggarwal, B. Allen, S. M. Aston, P. Aufmuth, S. Babak, M. A. Barton, C. Baune, C. Bell, C. Biwer, J. K. Blackburn, L. Blackburn, C. Bond, R. Bork, J. E. Brau, T. Chalermongsak, S. J. Chamberlin, N. Christensen, Q. Chu, C. Collette, M. W. Coughlin, S. Countryman, S. G. Crowder, M. Damjanic, K. Danzmann, H. Daveloza, W. Del Pozzo, T. P. Downes, M. Edwards, S. S. Eikenberry, L. Gondan, K. Gushwa, E. D. Hall, J. Hanks, I. W. Harry, S. Hee, M. Huynh, F. Jiménez-Forteza, K. Haris, G. Kang, H. Kaufer, W. Kells, C. Kim, S. Klimenko, J. Kline, L. Kuo, P. Leaci, C. H. Lee, J. R. Leong, A. L. Lombardi, F. Magaña-Sandoval, M. Mageswaran, Z. Márka, F. Matichard, L. Matone, K. McLin, M. Meinders, C. Mishra, S. R. Morris, A. Mullavey, T. Nash, M. E. N. Normandin, J. O'Dell, W. Ortega, O. Palashov, M. A. Papa, A. Pele, M. Pitkin, L. Prokhorov, E. Quintero, N. A. Robertson, G. Romanov, V. Sandberg, J. Scheuer, A. S. Sengupta, Z. Shao, B. Shapiro, D. H. Shoemaker, D. Simakov, A. Singer, A. Staley, J. Stebbins, D. Talukder, M. Tápai, M. P. Thirugnanasambandam,

E. Thrane, V. Tiwari, G. Vajente, J. Veitch, W. D. Vousden, A. R. Wade, L. Wen, J. T. Whelan, L. Williams, R. Williams, B. Willke, W. Winkler, L. Zhang, and Y. Zhang, *Advanced ligo, Classical and quantum gravity* **32**, 74001 (2015).

- [3] R. Adhikari, A. Brooks, B. Shapiro, R. Bhatt, D. McClelland, F. Carcoba, A. Markowitz, M. Laxen, E. Gustafson, V. Mitrofanov, K. Arai, Y. Michimura, C. Wipf, and E. Bonilla, *LIGO Voyager Upgrade: Design Concept*, Tech. Rep. (LIGO Scientific Collaboration, 2024).
- [4] M. Punturo, M. Abernathy, F. Acernese, N. Andersson, B. Barr, M. Barsuglia, M. Beker, N. Beveridge, S. Bose, L. Bosi, S. Braccini, C. Bradaschia, T. Bulik, E. Calloni, E. C. Mottin, S. Chelkowski, A. Chincarini, J. Clark, E. Coccia, C. Colacino, J. Colas, A. Cumming, L. Cunningham, E. Cuoco, S. Danilishin, K. Danzmann, R. De Salvo, T. Dent, R. De Rosa, L. Di Fiore, A. Di Virgilio, M. Doets, V. Fafone, P. Falferi, R. Flaminio, J. Franc, F. Frasconi, A. Freise, P. Fulda, G. Gemme, A. Gennai, A. Giazotto, K. Glampedakis, M. Granata, H. Grote, G. Guidi, M. Hannam, J. Harms, M. Hendry, E. Hennes, S. Husa, S. Huttner, G. Jones, K. Kokeyama, B. Krishnan, M. Lorenzini, H. Lück, E. Majorana, I. Mandel, C. Michel, Y. Minenkov, N. Morgado, B. Mours, P. Murray, C. D. Ott, C. Palomba, A. Paoli, G. Parguez, D. Passuello, L. Pinard, R. Poggiani, P. Popolizio, M. Prato, P. Puppo, D. Rabeling, J. Read, T. Regimbau, L. Rezzolla, F. Ricci, F. Richard, S. Rowan, A. Rüdriger, B. Sassolas, B. Sathyaprakash, P. Seidel, F. Speirits,

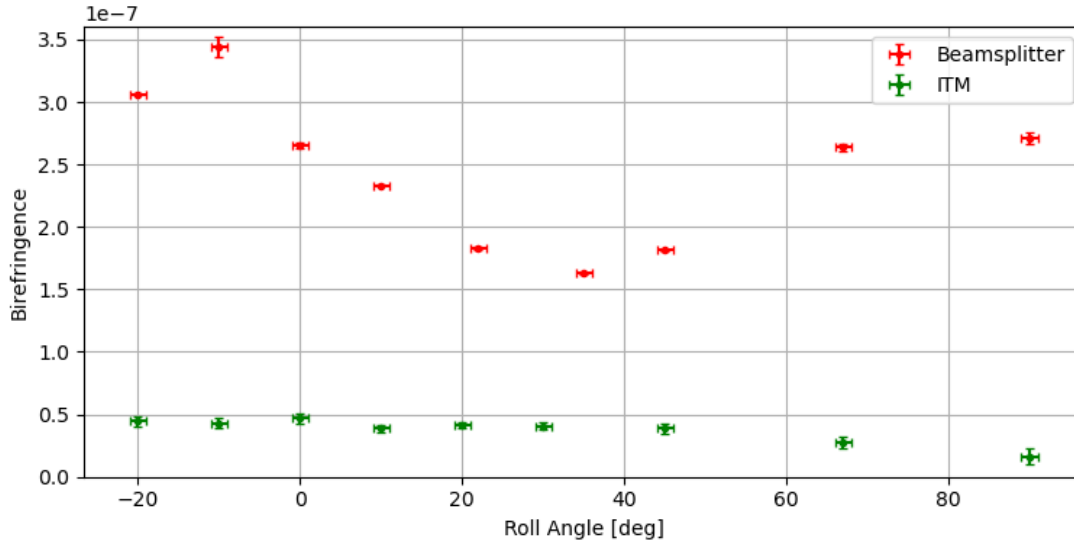


Figure 9: Measured averages of test mass central region. Points in red show the test mass in a beamsplitter configuration and the green shows measurements of the test mass in an ITM configuration. The ITM configuration gives a background birefringence due to external and internal stress of the test mass. It can be seen that this background birefringence does not have a strong angular dependence. The beamsplitter configuration demonstrates a clear minimum at 35° and maximum at -10° .

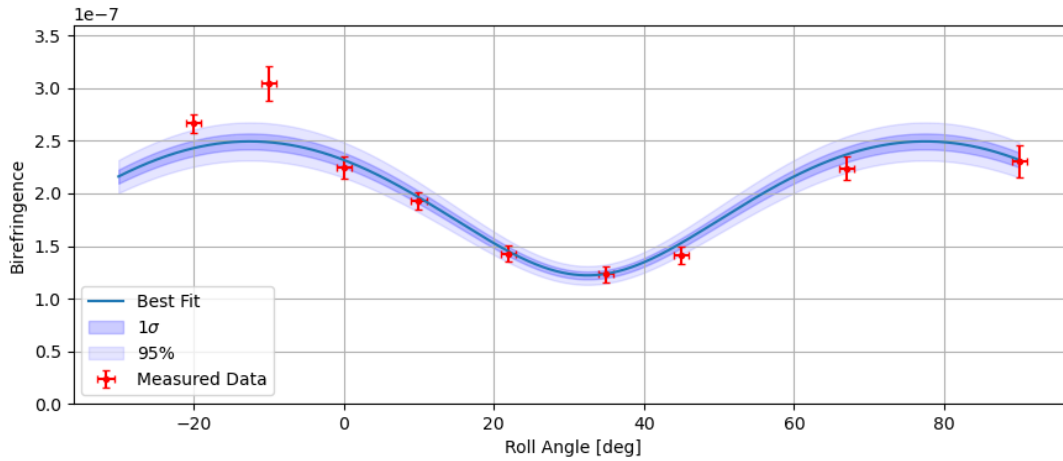


Figure 10: Shows the fit (in blue) with the measured birefringence with background birefringence subtracted. The bands give the standard error and 95% confidence interval of the fit value for the amplitude of the maximum birefringence. The fit was carried out on the data between -20° and 90° . This gave a value of $1.64 \pm 0.5 \times 10^{-6}$ for the maximum birefringence.

- K. Strain, P. Sutton, S. Tarabrin, C. van Leewen, M. van Veggel, A. Vecchio, J. Veitch, F. Vetrano, A. Vicere, S. Vyatchanin, B. Willke, G. Woan, P. Wolfango, and K. Yamamoto, The einstein telescope: a third-generation gravitational wave observatory, *Classical and quantum gravity* **27**, 194002 (2010).
- [5] M. Agathos, K. Agatsuma, P. Astone, G. Ballardin, F. Barone, M. Barsuglia, A. Basti, M. Bejger, M. Boer, F. Bondu, L. Bonelli, R. Bonnand, C. Bradaschia, A. Brillet, V. Brisson, T. Bulik, D. Buskulic, C. Buy, G. Cagnoli, E. Calloni, F. Cavalier, E. Cesarini, E. Chassande-Mottin, E. Coccia, P.-F. Cohadon, A. Colla, A. Conte, E. Cuoco, S. D'Antonio, M. Davier, R. Day, G. Debreczeni, J. Degallaix, M. De Laurentis, W. D. Pozzo, R. De Rosa, L. D. Fiore, A. D. Lieto, M. Drago, G. Endrőczy, V. Fafone, S. Farinon, F. Fidecaro, I. Fiori, R. Flaminio, J.-D. Fournier, S. Frasca, F. Garufi, A. Gatto, E. Genin, R. Gouaty, P. Groot, G. Hemming, R. J. G. Jonker, A. Królak, C. Lazzaro, E. Lebigot, M. Leonardi, N. Leroy, V. Lorientte, N. Man, M. Mantovani, F. Marchesoni, F. Marion, D. Meacher, J. Meidam, C. Michel, A. Moggi, M. Mohan, I. Neri, F. Nocera, C. Palomba, A. Pasqualetti, G. Pillant, L. Pinard, R. Poggiani, M. Punturo, P. Puppo, I. Rácz, M. Razzano, V. Re, F. Robinet, A. Rocchi, L. Roland, R. Romano, P. Ruggi, B. Sassolas, N. Straniero, M. Tonelli, F. Travasso, G. Vajente, N. van Bakel, M. van Beuzekom, C. V. D. Broeck, M. V. van der Sluys, G. Vedovato, J. Veitch, F. Vetrano, A. Viceré, and J.-P. Zendri, The advanced virgo detector, in *Journal of Physics: Conference Series*, Vol. 610 (IOP Publishing, Bristol, 2015) pp. 12014–.
- [6] Y. Levin, Internal thermal noise in the ligo test masses: A direct approach, *Physical review. D, Particles and fields* **57**, 659 (1998).
- [7] R. Nawrodt, A. Zimmer, T. Koettig, C. Schwarz, D. Heinert, M. Hudl, R. Neubert, M. Thürk, S. Nietzsche, W. Vodel, P. Seidel, and A. Tünnermann, High mechanical q-factor measurements on silicon bulk samples, *Journal of physics. Conference series* **122**, 012008 (2008).
- [8] T. Middelmann, A. Walkov, G. Bartl, and R. Schödel, Thermal expansion coefficient of single-crystal silicon from 7 k to 293 k, *Phys. Rev. B* **92**, 174113 (2015).
- [9] C. Krüger, D. Heinert, A. Khalaidovski, J. Steinlechner, R. Nawrodt, R. Schnabel, and H. Lück, Birefringence measurements on crystalline silicon, *Classical and quantum gravity* **33**, 15012 (2016).
- [10] V. M. V. M. Agranovich and V. L. V. L. Ginzburg, *Crystal optics with spatial dispersion, and excitons*, 2nd ed., Springer series in solid-state sciences ; v. 42. (Springer-Verlag, Berlin ;, 1984).
- [11] J. H. Burnett, Z. H. Levine, E. L. Shirley, and J. H. Bruning, Symmetry of spatial-dispersion-induced birefringence and its implications for, *Journal of Micro Nano lithography MEMS and MOEMS* **1**, 213 (2002).
- [12] J. Pastrnak and K. Vedam, Optical anisotropy of silicon single crystals, *Phys. Rev. B* **3**, 2567 (1971).
- [13] J. Burnett, Z. Levine, and E. Shirley, Intrinsic birefringence in calcium fluoride and barium floride, *Physical Review B* (2001).
- [14] T. Chu, M. Yamada, J. Donecker, M. Rossberg, V. Alex, and H. Riemann, Optical anisotropy and strain-induced birefringence in dislocation-free silicon single crystals, *Materials Science and Engineering: B* **91-92**, 174 (2002).
- [15] V. Jaberian Hamedan, A. Adam, C. Blair, L. Ju, and C. Zhao, Precision mapping of a silicon test mass birefringence, *Applied physics letters* **122** (2023).